Polarization and phase pulse shaping applied to structural contrast in nonlinear microscopy imaging

Peter Schön,[*] Martin Behrndt,[†] Dora Aït-Belkacem, Hervé Rigneault, and Sophie Brasselet
Institut Fresnel, MOSAIC, CNRS, Aix-Marseille Université, Ecole Centrale Marseille, Domaine Universitaire St Jérôme, F-13013 Marseille, France

(Received 26 May 2009; published 15 January 2010)

The spectral polarization shaping of ultrashort pulses is shown to allow retrieval of two-dimensional individual tensorial components of the second-harmonic-generation response of molecular samples in nonlinear microscopy imaging. This configuration, which cannot be performed by traditional polarization-controlled excitation, provides a structural contrast that can be directly related to information on the local symmetry and order of the sample, with submicrometric spatial resolution. Phase shaping, in addition to polarization spectral manipulation, is proposed as a possible scheme for imaging individual tensorial components without the need for a spectral information extraction.

DOI: 10.1103/PhysRevA.81.013809 PACS number(s): 42.65.Ky, 42.65.Re, 42.70.Mp

I. INTRODUCTION

Since its introduction as a possible analytical and structural measurement tool in molecular [1] and biomolecular [2] media, second harmonic generation (SHG) has been considerably developed. In particular SHG microscopy, first applied to crystals [3] and tissues [4], is now widely used in bio-imaging with prospects for biomedical diagnostics. Due to its inherent second-order nonlinear origin, coherent SHG only occurs in media exhibiting a noncentrosymmetry, which makes it a structural contrast by nature. Although microscopic-scale cross sections are lower than in two-photon fluorescence, SHG is a coherent process and thus leads to measurable signals in small focal volumes thanks to the efficient coherent buildup of nonlinear radiation from ordered individual emitters. SHG microscopy also benefits from the intrinsic advantages of multiphoton imaging, including less illumination scattering, deeper optical penetration, and intrinsic spatial resolution (typically 300 nm lateral) from nonlinear infrared excitations. SHG imaging has been developed in organic media from molecular monolayers [5,6] down to single micro- and nanocrystals [7–9], as well as labeled artificial and cell lipid membranes [10,11]. Intrinsic SHG responses from biomolecular assemblies such as in collagen [12–14], microtubules [15], and skeletal muscles [16] are now exploited with the ultimate goal of developing diagnostics of pathological effects related to tissues and cell architecture.

Besides the imaging capability of SHG, interesting properties are also contained in its polarization dependency. Manipulating the excitation polarization state in nonlinear microscopy can lead to fascinating effects, from spatial resolution enhancement [17,18] to enriched three-dimensional light-matter SHG interactions [19–21]. Today these possibilities benefit from various schemes of polarization manipulation [19,21], including polarization spatial shaping [22]. Polarization-resolved SHG imaging has been applied to retrieve molecular orientation information from highly ordered materials such as crystals [7–9,23–25], oriented molecular systems [6,26], and biological samples [27–31]. An adequate control of the polarization in SHG excitation-detection schemes allows one to distinguish the local nature (symmetry and orientational disorder) of molecular assemblies, which provides determining information for nano-material engineering as well as biological functional imaging. Symmetry and orientation information is contained in the nonlinear SHG tensorial coefficients $\chi^{(2)}_{IJK}$ [with (I, J, K) along the macroscopic frame axes (X, Y, Z)]. Polarization-resolved SHG imaging, however, suffers from a strong limitation, which is the impossibility to retrieve such coefficients individually without polarization tuning and additional data processing. Any incident polarization indeed leads to the measurement of a linear combination of the tensorial coefficients $\chi^{(2)}_{IJK}$. Developing a scheme which allows individual coefficient imaging would be beneficial to the exploration of samples of complex symmetry [27,32], contrast optimization, or identification of deviations from the Kleinman conditions where index permutations are no longer valid [31].

In this work, we use the capability of spectral pulse shaping to control the polarization, in addition to the phase, of an ultrashort pulse over its large spectral width, in order to both readout and control structural information from second-order nonlinear microscopy imaging in organized samples. Polarization shaping was first introduced as an additional degree of control in the optimization of two-photon excitation processes in gases [33–36] where the sharp spectral bands of anisotropic or aligned atomic transitions are adapted to polarized coherent control operations. Polarization optimization has also been applied in the correction of the polarization distortion in fiber propagation [37], coherent anti-Stokes Raman scattering nonresonant background rejection [38], and field localization on plasmonic nanostructures [39]. Various polarization-shaping schemes have been developed relying on the birefringence tuning of liquid-crystal modulators placed at the Fourier plane of a pulse shaper [40–45]. Here we show that polarization shaping can be applied to nonlinear microscopy for molecular structural order imaging, to ultimately enhance structural contrasts. To demonstrate the feasibility of this technique for individual SHG component retrieval, we illustrate polarization-shaping sum-frequency-generation (SFG)

[*]sophie.brasselet@fresnel.fr
[†]Current address: Max Planck Institute of Molecular Cell Biology and Genetics, D-01307 Dresden, Germany.

 ©2010 The American Physical Society

microscopy on an oriented crystal of known symmetry (Sec. II). The imaging capability of individual component retrieval is applied to the readout of the local disorder in a molecular crystal (Sec. III). Lastly, optimization schemes of polarization-resolved SFG excitation are investigated using phase shaping in addition to polarization control (Sec. IV).

II. TENSORIAL $\chi^{(2)}$ COMPONENTS READOUT USING PULSE SHAPING

A. Principle

The specificity of the nonlinear susceptibility tensor $\chi^{(2)}$ in SFG is to couple electric field components in a coherent and multidimensional scheme. Similar to phase control, an excitation with an ultrashort pulse containing a wide range of incident frequencies leads to various two-photon excitation pathways depending on the spectral profile of both phase and polarization states. The resulting intrapulse interference leads to the following expansion of the $I = (X, Y, Z)$ component of the induced nonlinear polarization:

$$P_I^{2\omega} = \sum_{JK=(X,Y,Z)} \int_\Omega \chi^{(2)}_{IJK}(\omega, \Omega) E_J(\omega - \Omega) E_K(\omega + \Omega)\, d\Omega, \tag{1}$$

where $\chi^{(2)}$ is a third-rank tensor with 27 components, and $E_J(\omega)$ the frequency dependence of the J incident polarization component of the field. In the case where no one-photon resonance is involved in the excitation process, the $\chi^{(2)}_{IJK}(\omega, \Omega)$ dependence appearing in Eq. (1) reduces to $\chi^{(2)}_{IJK}(\omega)$ where all two-photon excitation pathways have a similar interaction with the sample with respect to phase. We limit the present study to the case in which the spectral control does not involve intermediate electronic excitation levels. In addition, excitation conditions far from two-photon resonances lead to a ω-independent tensor $\chi^{(2)}_{IJK}$ where permutation of its three indices is allowed (Kleinman conditions). Polarization shaping consists in controlling independently the $E_J(\omega)$ amplitude and/or phase spectral dependence.

In the usual configuration of a two-photon excitation microscope, the sample lies in the (X, Y) plane which contains the polarization excitation components (X denotes here the horizontal polarization axis in the sample plane). In the case of a crystal, the $\chi^{(2)}_{IJK}$ coefficients depend on both its orientation defined by the Euler set of angles (ϕ, θ, ψ) and its symmetry defined by the set of microscopic $\chi^{(2)}_{ijk}$ components expressed in the unit-cell coordinate frame (x, y, z):

$$\chi^{(2)}_{IJK}(\phi, \theta, \psi) = \sum_{ijk=(x,y,z)} (\vec{I} \cdot \vec{i})(\vec{J} \cdot \vec{j})(\vec{K} \cdot \vec{k})(\phi, \theta, \psi) \chi^{(2)}_{ijk}, \tag{2}$$

where the $(\vec{I} \cdot \vec{i}), (\vec{J} \cdot \vec{j}), (\vec{K} \cdot \vec{k})$ factors are the (ϕ, θ, ψ)-dependent cosine directors of the microscopic frame relative to the macroscopic one. A typical orientational disorder can be expressed as the coherent superposition of nonlinear dipoles within a distribution of orientations (ϕ, θ, ψ). This leads to new macroscopic tensorial coefficients:

$$\chi^{(2)}_{IJK} = \iiint_{(\phi,\theta,\psi)} \chi^{(2)}_{IJK}(\phi, \theta, \psi) f(\phi, \theta, \psi) \sin\theta\, d\phi\, d\theta\, d\psi, \tag{3}$$

with $f(\phi, \theta, \psi)$ being the orientational distribution probability function of the crystal unit cells in the sample. This formulation shows that in the case of a purely one-dimensional (1D) crystalline sample (with only one nonvanishing coefficient $\chi^{(2)}_{zzz}$ in the microscopic frame) oriented along a macroscopic axis, the presence of orientational disorder can lead to significant nondiagonal macroscopic coefficients (such as $I = J \neq K$ and permutations).

To access the two-dimensional (2D) macroscopic nonlinear coefficients $\chi^{(2)}_{IJK}$ individually (with $I, J, K = X, Y$), the simplest scheme is to differentiate spectrally the two X and Y incident field components. A spectrally broad laser pulse is shaped in amplitude so that only two spectral windows remain, of which one, centered on ω_X, is polarized along X and the other, centered on ω_Y, is polarized along Y. Three coupling schemes are therefore possible, leading to three distinct peaks in the SFG spectrum: the first at $2\omega_X$ coupling E_X with itself, the second at $(\omega_X + \omega_Y)$ coupling E_X with E_Y, and the third one at $2\omega_Y$ coupling E_Y with itself [Figs. 1(a) and 1(b)]. In the plane-wave approximation (see discussion below in Sec. II D), the detected intensity along the $I = (X, Y)$

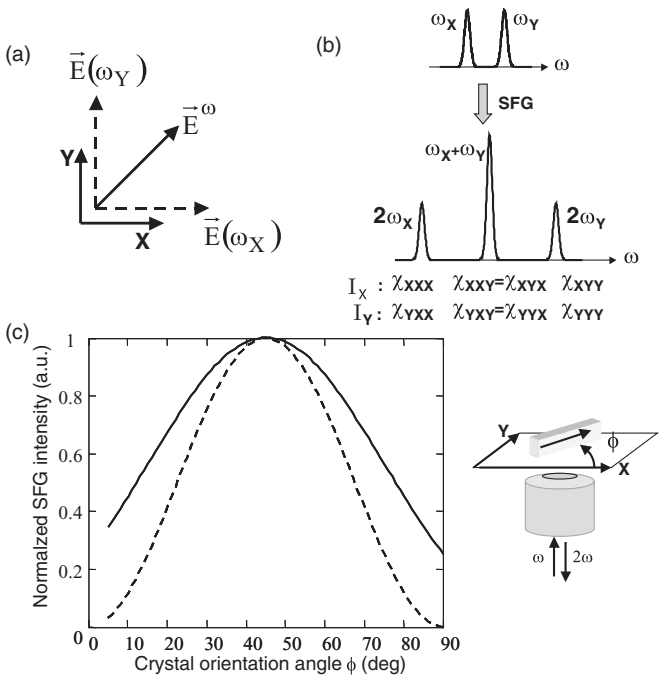

FIG. 1. Comparison between polarization shaping and linear polarization excitations for a 1D nonlinear crystal lying in the (X, Y) plane of the sample with a variable ϕ orientation angle relative to X. (a) Field excitation scheme. (b) Spectra of the incident and SFG components in the polarization-shaping scheme. (c) SFG total intensity $I_X + I_Y$. Continuous line: excitation by a single frequency field polarized along the 45° direction relative to X. Dashed line: excitation by the polarization-shaped field described in (b), detection of the spectral component extracting the coupled $\chi^{(2)}_{XXY}$ component of the signal.

analysis direction is proportional to $|P_I|^2$. The resulting SFG spectrum along I contains therefore three spectrally separated components centered on $(\omega_J + \omega_K)$, proportional to $|\chi^{(2)}_{IJK}|^2$. The amplitude of the central peak representative of the XY coupling is consequently $4|\chi^{(2)}_{IXY}|^2$ due to the possible X and Y permutation. If the SFG radiated fields are separated according to their polarization components in X and Y, the resulting six peaks of the spectral intensity measurement therefore give access independently to $\chi^{(2)}_{XXX}$, $\chi^{(2)}_{XYX} = \chi^{(2)}_{XXY}$, $\chi^{(2)}_{XYY}$, $\chi^{(2)}_{YXX}$, $\chi^{(2)}_{YXY} = \chi^{(2)}_{YYX}$, and $\chi^{(2)}_{YYY}$.

Contrary to a single-incident polarization scheme, all components can be therefore sorted out independently without being mixed with each other. A polarimetric single-frequency measurement indeed addresses $P^{2\omega}_I = \sum_{JK=(X,Y,Z)} \chi^{(2)}_{IJK} E^{\omega}_J E^{\omega}_K$ and thus always leads to a linear combination of multiple coefficients whatever the incident polarization state. The benefit of using polarization shaping is illustrated in Fig. 1 where the two situations are compared for a 1D crystal in the (X, Y) sample plane. This crystal being of pure 1D symmetry, only one diagonal microscopic coefficient $\chi^{(2)}_{uuu}$ is involved, with u its main axis direction in the (X, Y) plane. Note that in this specific geometry, no coupling is involved in the Z direction even in the case of a high aperture angle focusing, since the nonlinear tensor does not contain any Z index components. More complex situations involving Z-coupling components are discussed in Sec. II D. The polarization-shaping readout of the SFG $(\omega_X + \omega_Y)$ signal is seen to provide a better contrast with respect to the crystal orientation. Indeed, for a given linear polarization (here 45° relative to X), all crystal orientations give a nonvanishing signal, whereas for a polarization-shaping readout, the SFG signal drops down to zero when the crystal lies along X or Y, since only individual $\chi^{(2)}_{IXY}$ coefficients are detected. In this specific example, a crystal oriented at $\phi = 45°$ therefore shows an optimum contrast relative to other crystal orientations. This illustration can be transposed to any other ϕ angle.

B. Experimental

The polarization-shaping experimental design is based on the spatial separation of spectral components of the incident ultrashort pulse, further sent through spatial light modulators (SLM) consisting of controllable arrays of birefringent liquid crystals (LCs) [40–45].

On this basis, several schemes are possible:

Phase and amplitude shaping. After being sent through a polarizer along X, the beam traverses two LC arrays whose axes are inclined at 45° relative to the polarizer direction, so that the ordinary axis of the first array corresponds to the extraordinary axis of the second and vice versa. Another polarizer in the same direction as the first one is placed at the exit of the device. This leads to an expression for the transmitted field E_1 which only depends on the phase shifts $\Delta\Phi'$ and $\Delta\Phi''$ introduced, respectively, by the first and second LC array:

$$E_1 \propto E_0 \cos\left(\frac{\Delta\Phi'' - \Delta\Phi'}{2}\right) e^{i\frac{\Delta\Phi'' + \Delta\Phi'}{2}}, \tag{4}$$

with E_0 the input field amplitude. The control of both phase shifts determines the amplitude of the transmitted field E_1 (by their difference) and its phase (by their sum), therefore allowing for independent amplitude and phase shaping.

Polarization shaping. The beam passes through a single LC array whose axes are again inclined 45° to the entrance polarizer direction along X, with no additional polarizer at the exit. Achievable polarization states range successively from linear along X for a phase shift $\Delta\Phi = 0°$ introduced in the LC, to elliptical with a major axis along X $(0° < \Delta\Phi < 90°)$, to circular $(\Delta\Phi = 90°)$, to elliptical with a major axis along Y $(90° < \Delta\Phi < 180°)$, and finally to linear along Y $(\Delta\Phi = 180°)$. The output field E_2 components in the (X, Y) frame are therefore

$$E_2 \propto \sqrt{2} E_1 e^{i\frac{\Delta\Phi}{2}} \begin{bmatrix} i \sin\dfrac{\Delta\Phi}{2} \\ \cos\dfrac{\Delta\Phi}{2} \end{bmatrix}. \tag{5}$$

This scheme allows in particular the creation of pulse profiles with regions of frequencies that are linearly polarized perpendicular to one another. The combination of a dual and a single LC permits one to manipulate independently the amplitude, phase, and polarization of the excitation field.

The setup is shown in Fig. 2. A Ti:sapphire laser delivering pulses around $\lambda = 800$ nm with a full width at half maximum (FWHM) of 60 nm is used for all experiments. In a $4f$ geometry, a diffraction grating (600 lines/mm) spatially separates the spectral components that are reflected by a planar mirror onto a spherical one, which creates again a parallel beam. Two LC devices (one dual two-array SLM for phase and amplitude control, and one single-array SLM for polarization control, each with 640 nematic liquid-crystal pixel elements) are inserted at the focal distance of the spherical mirror, after which the beam gets recombined by an identical setup of spherical mirror, planar mirror, and diffraction grating to pass through the same pinhole as the ingoing beam. The large focal length of the spherical mirrors (500 mm) allows a large Rayleigh distance in the Fourier plane and therefore a less stringent positioning of the SLMs in the propagation direction. This pulse shaper design leads to a dispersion of 0.3 nm per pixel in the SLM planes. The

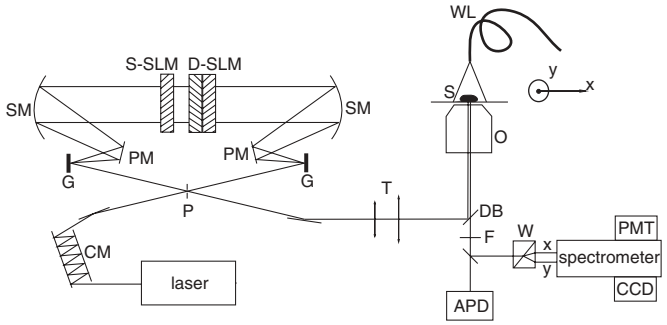

FIG. 2. Experiment setup. CM: chirped mirrors; P: pinhole; G: diffraction gratings; PM: plane mirror; SM: spherical mirror; D/S-SLM: dual/single SLM; T: telescope; DB: dichroic beam splitter; O: objective; S: sample; WL: white light illumination; F: visible light bandpass filter; W: Wollaston prism; PB: polarizing beam splitter; APD: avalanche photodiode; PMT: photomultiplier tube.

relatively low line density of the gratings is chosen to ensure a similar reflectivity for horizontally and vertically polarized light (a 15% reflectivity difference is measured between those components). The overall transmission of the pulse shaper for horizontally polarized light is 15%. Before being sent through a high numerical aperture (NA) (water immersion, NA = 1.2) objective to the sample, a telescope enlarges the beam to completely fill the objective's back aperture. The incident power, integrated over the whole spectrum, is of the order of a few mW in the sample plane. The emitted SFG signal from the sample is collected by the same objective and separated from the incoming laser beam by a dichroic beam splitter and a bandpass filter in the visible region. The dichroic beam splitter is chosen for its low group velocity dispersion as well as its low polarization dichroism factor in the 720–880 nm spectral region. For calibration and phase optimization experiments, the SFG signal is collected in the epi direction by an avalanche photodiode (APD). For spectral measurements, the SFG signal is sent to a spectrometer. Separated X and Y component detection is performed by inserting a Wollaston prism into the entrance slit and imaging the spectrum on two separate regions of a CCD camera chip. For individual SFG tensorial component imaging, specific wavelengths of the spectrum are detected by a photomultiplier tube placed in front of a monochannel exit slit. Additionally in this microscope, white light illumination is used to image the orientation of macroscopic objects.

For polarization shaping only, the experiment requires a spectrally flat phase at the focal spot of the objective. A first compensation for the large second-order frequency dependence introduced by the group velocity dispersion of the objective, lenses, and mirror reflections is performed by a pair of chirped mirrors in a multiple reflection scheme into the beam path. As a merit function for the attainment of a spectrally flat phase, we measure a nonlinear two-photon excitation process, here the two-photon fluorescence (TPF) intensity of a solution of rhodamine 6G placed in the sample plane detected by the APD. A flat phase throughout the laser pulse spectrum corresponds to a Fourier transform limited pulse, meaning the shortest in the time domain, and the most efficient for two-photon excitation. At this stage, a 40-fs FWHM time width is measured by autocorrelation [46]. Further remaining phase distortions are corrected directly using the pulse shaper in a pure phase-correction mode. The pulse spectral profile is optimized without *a priori* knowledge of its nature by an evolutionary strategy as described in Refs. [47–50].

We follow this approach by measuring the TPF signal for 100 random pulse-shaper configurations of which we choose the 15 best ones which become the parents for the next generation. Those are recombined to create a new population of 100 configurations in a way that for each of those children, we select two of the parents and take for each element of the child the corresponding SLM voltage value of one of the parents. All children are then mutated by adding a Gaussian noise to each of the elements, to provide a means to jump out of local minima in the configuration space. After measuring the whole population the best 15 are chosen again, and the procedure repeats itself. A self-adaptive mutation width is introduced in order to adapt to the fact that in the beginning a relatively large area of the configuration space should be explored, while later on, when the region of the presumably global minimum has been narrowed, the search should be focused. Whenever 60% of the young population gives a higher signal than their parents, the width of the Gaussian used for the mutation of the next generation decreases by 10%, otherwise it increases by the same percentage [50]. After about 300 generations, a stable maximum in the TPF intensity is seen to be reached. The resulting configuration can then be considered to correct for the remaining phase distortions and to lead to a spectrally flat phase.

C. Results

The individual SFG tensorial component readout is first performed on a crystal of known symmetry and orientation. A macroscopic $KTiOPO_4$ crystal (KTP) is placed with its $(1, 3) = (x, z)$ crystallographic plane in the microscope's sample plane. No resonances lie within the incident wavelength range, and in this regime the nonlinear components are $\chi^{(2)}_{zzz} = 33.8$, $\chi^{(2)}_{zxx} = 5.08$, and $\chi^{(2)}_{zyy} = 8.7$ pm/V [51]. The crystal can be rotated around its y axis (which is along the incident propagation direction Z), therefore allowing a variation of the macroscopic nonlinear coefficient as detailed in Eq. (2), with $\theta = 90^\circ$, $\psi = 90^\circ$, and ϕ variable, ϕ being defined as the angle between the crystal axis z and the X macroscopic axis. Two laser profiles are tested: in the first case, the whole spectral width of the pulse is sent to the sample with a flat spectral phase and polarized either along the X or the Y direction. In the second case, both spectral amplitude and polarization are shaped so that only two spectral windows of 10 nm width, centered on 780 and 820 nm, are, respectively, polarized along X and Y. The SFG spectra for those profiles are measured for different crystal orientations, which are estimated independently using white light illumination imaging.

Figure 3 displays the experimental results normalized to the maximal value of $\chi^{(2)}_{XXX}$ (obtained for $\phi = 0$) for both experimental configurations. The measurements are compared with the theoretical model based on Eqs. (1) and (2), in which the experimental angle ϕ is introduced as a variable parameter. A slight improvement of the agreement between the experimental and theoretical data is obtained by introducing two additional fitting factors: the ratio between the X and Y incoming field amplitudes, and the ratio between the X and Y detection channel efficiencies. First, the excitation dichroism factor η is introduced to account for the different amplitudes of the incoming field in its two polarization states such as $E_Y = \eta E_X$. This factor is mainly caused by the polarization-dependent reflection efficiency of the diffraction grating at the exit of the pulse shaper and by additional mirror reflections. Introducing η as a fitting parameter leads to $\eta = 1$ in Fig. 3(a) and $\eta = 0.7$ in Fig. 3(b). These factors are in agreement with the values obtained from separate measurements of the fundamental beam intensity at the entrance of the microscope for both X and Y polarization projections. Second, a detection dichroism factor is introduced to account for the detection efficiency difference between the two channels of the spectrometer, which is estimated at 0.8. This is in agreement with an independent estimation of this factor using the depolarized two-photon fluorescence emission

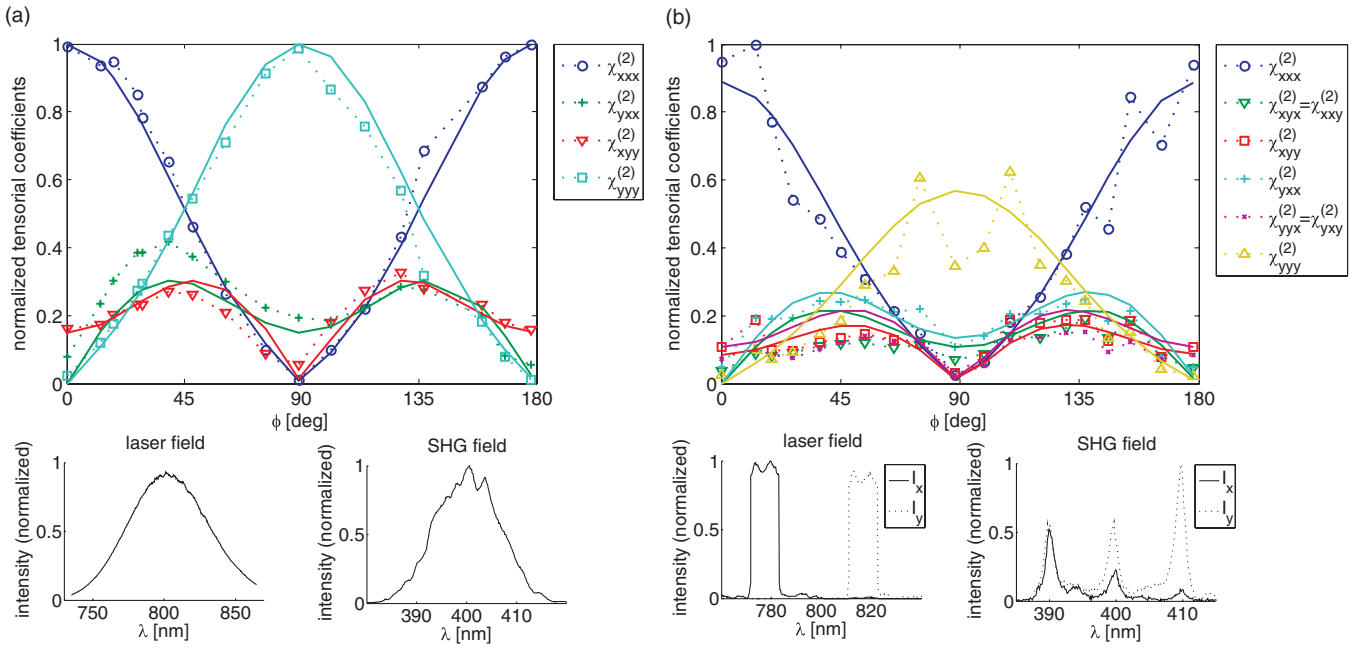

FIG. 3. (Color online) Dependence of the measured relative tensorial components of a KTP crystal with respect to its in-plane orientation angle ϕ. Dashed lines: experimental data; solid lines: expected behavior according to the calculations detailed in the text. (a) Whole spectrum polarized in one direction. (b) Two narrow spectral windows with perpendicular polarization to each other. Lower pictures: incident laser spectrum and corresponding measured SFG spectrum for both cases (the right-side spectrum is obtained for a KTP orientation of $\phi = 90^\circ$, with dotted (continuous) lines corresponding to a Y (X) analysis direction.

from a rhodamine 6G water solution placed on the sample stage. Both factors only affect the overall magnitude but not the shape of the orientation-dependence curves depicted in Fig. 3. Figures 3(a) and Fig. 3(b) show a good agreement with the expected SHG tensor coefficient dependence with respect to the ϕ macroscopic in-plane crystal orientation, with a maximum error margin of 30%. Figure 3(b) shows in particular that six individual coefficients of the crystal nonlinear susceptibility can be retrieved from a spectral filtering, which is based on a single pulse measurement. In contrast, the more traditional scheme of Fig. 3(a) requires two different measurements involving separate X and Y excitation polarizations. Whatever its direction, this single polarization excitation is unable to retrieve more than two crystalline SHG tensorial components. Although it is not visible in the present case where index permutations are valid since Kleinman conditions are applicable, this approach shows furthermore that polarization pulse shaping allows the investigation of possible deviations from index permutation conditions since six coefficients are determined independently, which is not the case with a single polarization excitation.

D. Effect of the Z-direction coupling under high aperture excitation and detection

The development above assumes pure incident polarization components in the (X, Y) plane similar to a plane-wave excitation. In practice in nonlinear microscopy, the use of a high numerical aperture (NA) objective modifies the polarization field conditions both for the excitation of the nonlinear medium as well as the detection of the generated signal. Strong focusing introduces in particular a component of the electric field along the incident light propagation direction Z and redistributes the lateral polarization for positions in the focal volume which do not lie on the optical axis [52]. For instance at NA = 1.2, the Z component of the excitation electric field reaches at its maximum 30% of the in-plane (X, Y) amplitude. This contribution can have a non-negligible effect in cases where the nonlinear coupling involves strong Z-index susceptibility components [53,54]. In addition when collecting the SHG signal with such an objective, the nonlinear radiation also mixes up polarization components which are coherently integrated over the objective aperture angle. The effect of the Z component on the polarized measurements depends on the symmetry of the studied system, therefore each case should be investigated specifically. To account for both excitation and collection effects, we developed a model which calculates the nonlinear radiation propagation in an assembly of excited dipoles in the focal volume, which then propagates in the detection optical system [54]. This approach, which encompasses both issues of excitation and detection polarization mixing components, allows one to model the sample rotation dependence such as shown in Fig. 3, accounting for all tensorial coefficients including their out-of-plane contributions. For any crystal orientation in the macroscopic frame, the Z-coupling contributions to the $\chi^{(2)}$ tensor can be quantified by the ratio between the part of the tensor norm containing Z components, i.e., $\chi^{(2)}_{\text{out}} = \sqrt{\sum_{I'J'K'}(\chi^{(2)}_{I'J'K'})^2}$ with I', J', K' containing at least once the Z coefficient, and the full norm $\chi^{(2)} = \sqrt{\sum_{(I,J,K)=(X,Y,Z)}(\chi^{(2)}_{IJK})^2}$. In the case of KTP, with axes $(1, 3) = (x, z)$ lying in the sample plane (X, Y), the

out-of-plane contribution ratio is $\chi^{(2)}_{\text{out}}/\chi^{(2)} = 0.26$. Turning the KTP main axis 3 along the Z direction increases this ratio to $\chi^{(2)}_{\text{out}}/\chi^{(2)} = 0.96$, as expected from the prominent Z coupling in this case. More generally, the magnitude of the out-of-plane nonlinear coupling can be quantified in any sample symmetry by the ratio $\chi^{(2)}_{\text{out}}/\chi^{(2)}$, which ranges between 0 (no Z coupling) and 1 (maximum Z-coupling effect).

Figure 4 shows the effect of the Z-coupling contributions on the KTP crystal rotation experiment detailed above (Fig. 3). Figure 4(a) shows the theoretical rms error between the situation NA = 1.2 and the plane-wave approximation in such an experiment, as a function of the ratio $\chi^{(2)}_{\text{out}}/\chi^{(2)}$. This error is seen to lie in a reasonable range (below 4%) for $\chi^{(2)}_{\text{out}}/\chi^{(2)} < 0.8$. Above this value, the error grows rapidly, which makes the determination of in-plane tensorial coefficients not reliable anymore. The maximum value reached by this error in the sample rotation dependence is represented in Fig. 4(b). Both figures show that the reliability of this experiment working at high numerical aperture (NA = 1.2) is guarantied for $\chi^{(2)}_{\text{out}}/\chi^{(2)} < 0.8$. The effect of a high out-of-plane coupling on the sample rotation dependence is exemplified for KTP in Figs. 4(c) and 4(d), in the extreme case $\chi^{(2)}_{\text{out}}/\chi^{(2)} = 0.96$, where the KTP crystal would have its major axis contribution along the Z direction. Strong modifications of the angular dependence are induced by the Z-coupling contribution for high numerical aperture focusing [Fig. 4(c), NA = 1.2]. However, using a lower aperture (NA = 0.5, which still provides reasonable micrometric resolution) is shown to be highly reliable even for samples containing significant Z-coupling contributions [Fig. 4(d)]. The use of a high-numerical-aperture objective can therefore be applied to the present experiment (assuming that a 4% error margin is acceptable) as long as the Z-coupling contribution to the tensor does not surpass 0.8, which can be reached in samples where the main symmetry axis lies along Z. In the general case of an unknown Z contribution, the use of a lower numerical aperture is relevant. Note that similar conclusions could be drawn for any other crystal or sample symmetry by using the $\chi^{(2)}_{\text{out}}/\chi^{(2)}$ ratio as a quantification of the Z-component contribution to the nonlinear coupling.

Finally in the present study developed in Sec. II C, the Z coupling in KTP involves only its $\chi^{(2)}_{zyy}$ susceptibility

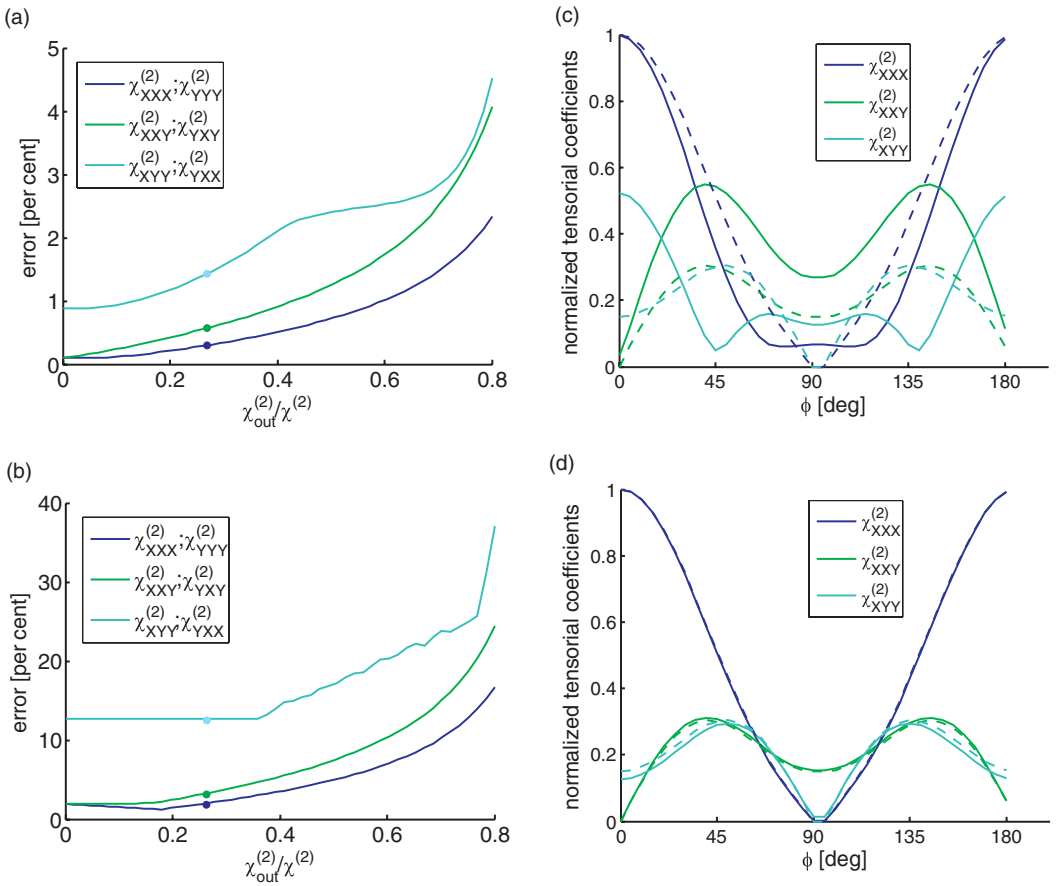

FIG. 4. (Color online) Effect of the out-of-plane Z contribution to the nonlinear coupling on the polarization-shaping experiment (theoretical calculations). (a) Theoretical rms error between the situation NA = 1.2 and the plane-wave approximation, estimated on the KTP rotation dependence (Fig. 3) of individual nonlinear tensorial components, as a function of the ratio $\chi^{(2)}_{\text{out}}/\chi^{(2)}$ which quantifies the amount of Z-coupling contribution. The points correspond to the situation of a KTP crystal with its (1, 3) axes in the sample plane. Components undergoing a similar dependence are joined in the same curve. (b) Maximum value reached by the error defined in (a). (c) Calculated KTP rotation dependence of the individual tensorial components in the case $\chi^{(2)}_{\text{out}}/\chi^{(2)} = 0.96$ (KTP main axis along Z) for NA = 1.2 (continuous line) and a plane-wave approximation (dashed line). (d) Same dependencies for NA = 0.5 (continuous line) and a plane-wave approximation (dashed line).

component, which is 30% of the main component $\chi^{(2)}_{zzz}$. The consequent Z-coupling efficiency therefore does not affect significantly the rotation-dependent data of Fig. 3. The maximum error margins in this situation are 1.8% for $\chi^{(2)}_{XXX}$ (measured at $\phi = 45°$), 3% for $\chi^{(2)}_{XYX}$ (at $\phi = 45°$), and 13% for $\chi^{(2)}_{XYY}$ (at $\phi = 90°$). The high numerical aperture focusing is thus seen to have a minor effect on the polarization responses, which is mainly due to the still low Z-coupling conditions in KTP. In addition, this estimated error range corresponds to the maximum discrepancy range obtained between the experimental and theoretical SHG-angle dependencies shown in Fig. 3.

Although the context of this work is the determination of relative nonlinear macroscopic coefficients of a sample projected in the (X, Y) sample plane, we also investigated the influence of the off-plane tilt angle θ of the sample on such an experiment to investigate its possible influence on the retrieved 2D information. θ is defined as the angle between the Z direction and the high symmetry axis of the sample (the 3 axis in the case of KTP). Theoretical calculations performed on KTP show that an off-plane rotation of the crystal can induce deviations to the expected coefficients at high tilt angles (typically θ below $\pi/8$) using a numerical aperture of 1.2 [Fig. 5(a)], whereas the use of a lower numerical aperture (0.5) does not alter the measured data significantly. This is essentially because the projection of the sample in the (X, Y) plane still keeps an important part of the symmetry information. This is also observed in the simulation of a polarization-shaping readout experiment where 2D coefficients are retrieved for a tilted KTP crystal [Fig. 5(c)]: the influence of the tilt angle in this case is seen to be negligible.

III. MOLECULAR ORDER IMAGING USING POLARIZATION PULSE SHAPING

As described above, individual SFG tensorial components contain valuable information on the nanometric scale structure of a molecular sample. Such components were previously measured using a polarimetric approach by continuously varying an incoming polarization state, which required long acquisition times and *a posteriori* extensive data treatments [9,23–25]. Here we propose an alternative to retrieve molecular order information from single SFG-component imaging. This measurement, based on polarization shaping, does not rely on a variable input polarization but rather on a single-pulse input excitation. Extracting independent SFG tensorial components by polarization pulse shaping can be extended to imaging using the same scheme as detailed in the previous section. Since imaging requires fast acquisition times which are not generally reached by a spectrometer, we extended the instrument to a single channel measurement integrating a spectral range in a fast photon-counting mode. Single $\chi^{(2)}$ component imaging is based on the extraction of the corresponding spectral regions of the detected spectrum, by detecting a small spectral window of $\Delta\lambda \approx 3$ nm around the corresponding SFG wavelength toward a photomultiplier tube through the single-channel exit slit of the spectrometer (Fig. 2). By setting the detected wavelength

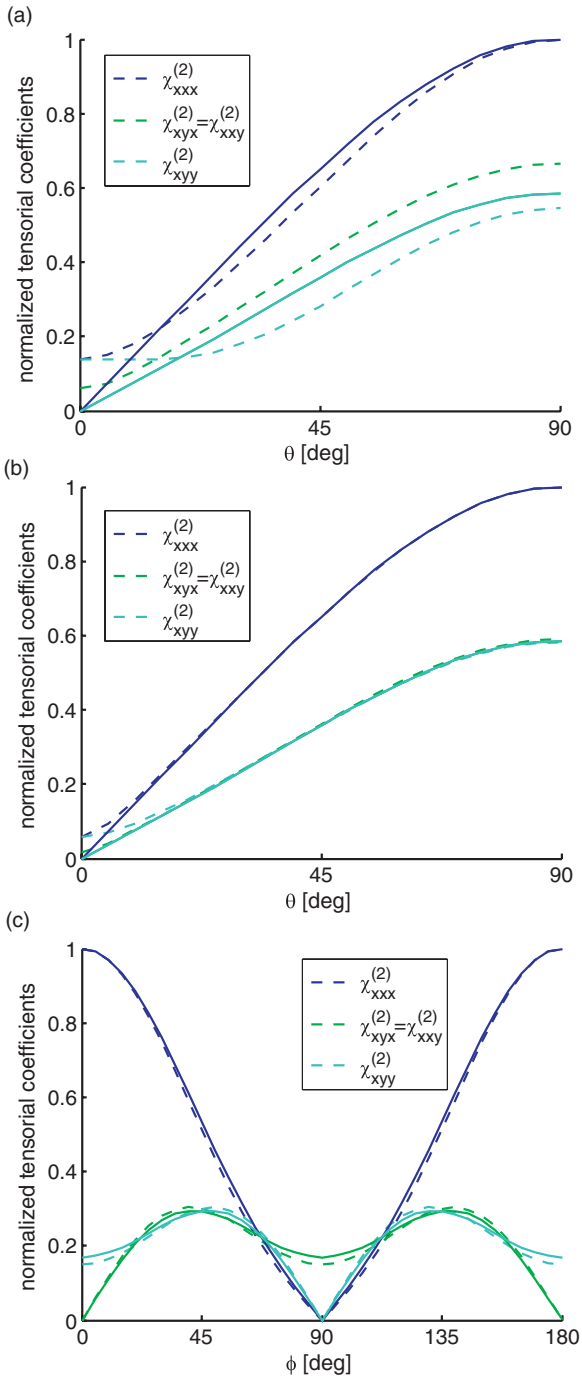

FIG. 5. (Color online) Effect of the out-of-plane θ tilt angle of the KTP crystal, on the polarization-shaping experiment (theoretical calculations). Components undergoing a similar dependence are joined in the same curve, as in Fig. 4. All the coefficients are normalized to $\chi^{(2)}_{XXX}$ measured at $(\phi = 0, \theta = \pi/2)$. (a) θ dependence of the individual KTP macroscopic nonlinear coefficients at $\phi = \pi/4$, for NA = 1.2 (dashed line) and in the plane-wave approximation (continuous line). (b) Same dependence for NA = 0.5 (dashed line) compared to the plane-wave approximation (continuous line). (c) ϕ rotation dependence of the KTP individual nonlinear tensorial components (such as measured in Fig. 3) for $\theta = \pi/2$ (dashed line) and $\theta = \pi/4$ (continuous line).

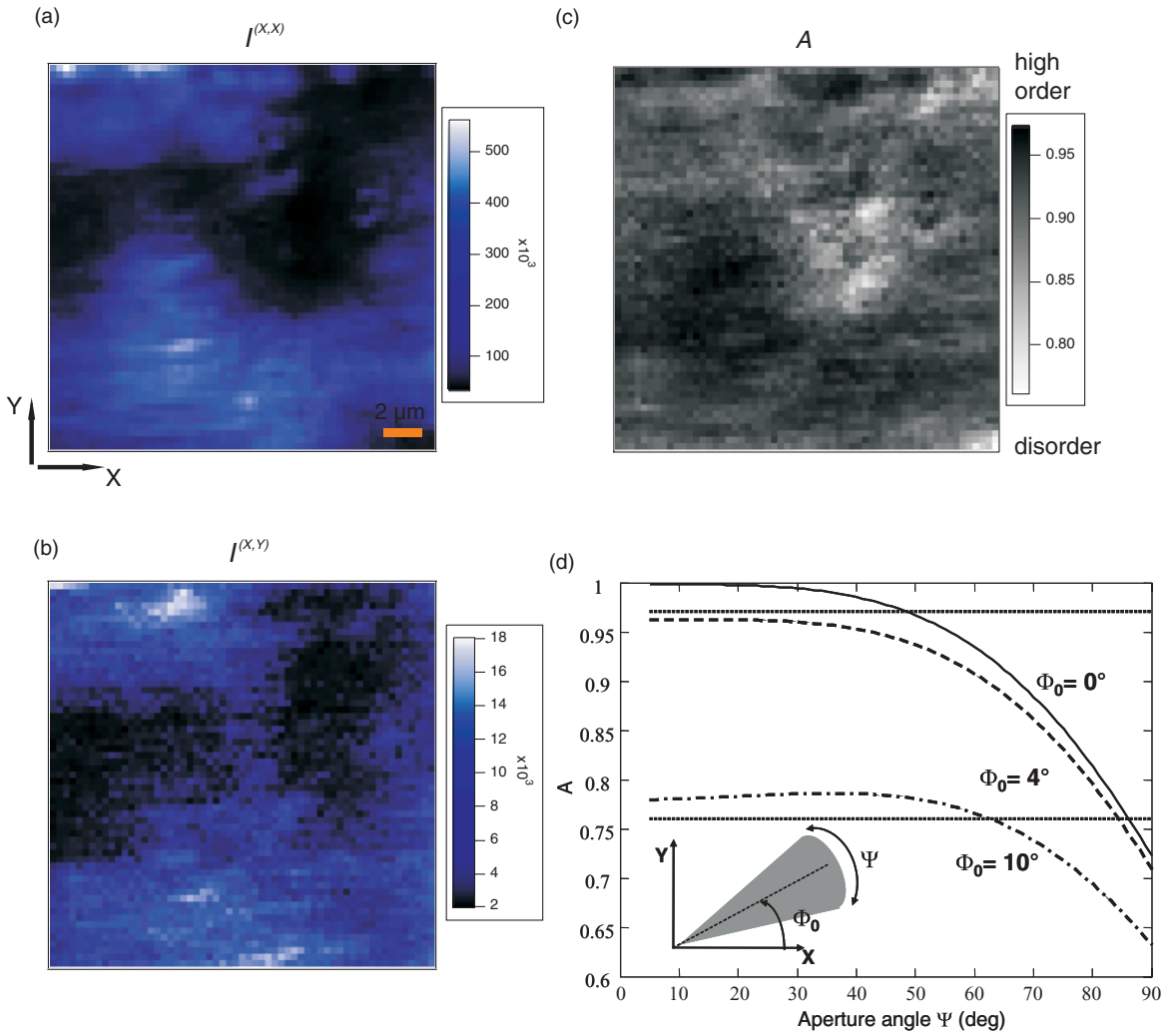

FIG. 6. (Color online) Imaging of tensorial components of a 1D symmetry DANS-PHTP crystal. (a) $I^{(X,X)}$ intensity component. (b) $I^{(X,Y)}$ intensity component (both in counts/s). (c) Anisotropy A as described in the text. (d) Calculation of the anisotropy A dependence as function of the angular aperture Ψ and the tilt angle of the cone Φ_0.

on $\omega_J + \omega_K$, an image is obtained for the corresponding $I^{(J,K)} = I_X^{(J,K)} + I_Y^{(J,K)}$ intensity defined above, leading to the measurement of $(4 - 3\delta_{JK})(|\chi^{(2)}_{XJK}|^2 + |\chi^{(2)}_{YJK}|^2)$ [the factor $(4 - 3\delta_{JK})$ being introduced to account for the XY permutation in the field coupling]. Separate $|\chi^{(2)}_{XJK}|^2$ and $|\chi^{(2)}_{YJK}|^2$ measurements are obtained by placing an analyzer at the entrance slit of the spectrometer. The imaging of independent components is demonstrated on a 1D symmetry crystal studied previously [25], made of the perfect alignment of nonlinear molecules 4-dimethylamino-4′-nitrostilbene (DANS) included by co-crystallization with perhydrotriphenylene (PHTP) (note that in this symmetry case the Z contribution discussed in Sec. II D is of minor influence). This crystal is placed with its main 3 axis along the X direction, as verified by white light illumination imaging and additional polarimetric measurements. This situation allows the identification of possible crystalline disorder as discussed in Sec. II. (X, X)- and (X, Y)-coupling components SFG images, depicted, respectively, in Figs. 6(a) and 6(b), show that the main tensorial component present in the crystal involves the (X, X) coupling represented by the dominant $I^{(X,X)}$ intensity, as expected from the sample symmetry. The presence of a weak but existing $I^{(X,Y)}$ contribution in several crystal regions is a signature of imperfect 1D alignment along the X axis at those locations. In order to quantify the local orientational disorder present in the crystal, we define the anisotropy factor $A = (I^{(X,X)} - I^{(X,Y)})/(I^{(X,X)} + I^{(X,Y)})$ which does not depend on the incident intensity [Fig. 6(c)]. A can be evaluated theoretically using a model where the crystal is made of a collection of microscopic molecular dipoles which are not strictly parallel to the crystal-axis direction. The angular distribution of these dipoles $f(\phi, \theta, \psi)$ is defined as a cone of angular aperture Ψ lying in the (X, Y) plane, tilted by an angle Φ_0 relative to X [Fig. 6(d)]. This distribution is used to calculate the macroscopic tensorial components $\chi^{(2)}_{IJK}$ from Eq. (3), further introduced in Eq. (1) to deduce the SFG intensities $I^{(X,X)}$ and $I^{(X,Y)}$. A quantifies the order in the sample, with in the present case $A = 1$ for a pure 1D crystalline orientation along X (high order), and $A = 0$ for a high disorder. This model shows that for a known cone orientation, the measurement of A leads to an estimation of the degree of

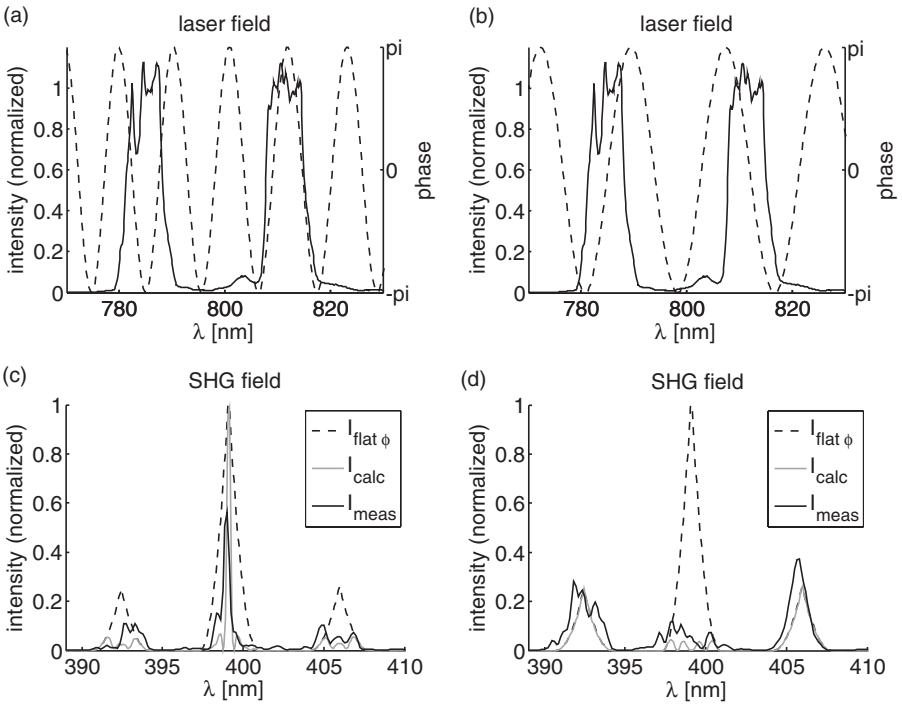

FIG. 7. Phase control of the different polarization coupling schemes following the design of odd vs even dependencies of the spectral phase in two spectral windows. (a) and (b): laser field with intensity (continuous line) and phase (dashed line). (c) and (d): their corresponding SHG spectra with the measured signal (black line), the expected signal (light grey line), and the expected signal for a flat spectral phase (dashed line) for comparison; symmetric phases in the spectral windows attenuate the side peaks leaving the one in the center [(a) and (c)], while antisymmetric phases in the spectral windows leave the side peaks and attenuate the central peak [(b) and (d)].

disorder (Ψ) of the molecular orientation in the crystal. The dependence of A relative to the cone aperture Ψ is seen to be shifted to lower A values when Φ_0 increases [Fig. 6(d)]. The lack of knowledge of a possible tilt angle Φ_0 of the cone does not prevent a qualitative estimation of the disorder (cone aperture). The maximum $A = 0.97$ value measured in the present crystal indeed leads to $\Phi_0 < 4^\circ$ and $\Psi < 50^\circ$, meaning that in the "high-order" regions, the measured molecular cone aperture angle cannot surpass 50°. The minimum $A = 0.76$ value measured on the crystal leads to $\Phi_0 < 10^\circ$ (which is expected in the present situation since the crystal is placed along X). Inspection of the cone aperture dependence leads to a disorder of $60^\circ < \Psi < 85^\circ$ in the regions identified as "highly disordered." Such behavior in the measured crystal has been previously observed in a complete polarimetric analysis [25].

IV. SINGLE SFG TENSORIAL COMPONENT CONTRAST USING PHASE AND POLARIZATION PULSE SHAPING

The possibility of manipulating intrapulse interferences by the design of specific spectral phase profiles has been exploited in molecular media to enhance nonlinear pathway efficiencies [55] and improve the contrast in two-photon coherent effects [56]. In addition to the polarization control detailed above, phase shaping could therefore provide an additional degree of control to enhance nonlinear processes related to a given symmetry inside a sample. Here we explore the possibility of annihilating polarization coupling pathways by phase shaping, with the perspective of a structural contrast imaging that would avoid the use of the spectral filtering described above.

A phase-shaping scheme involving the control of the parity of the phase profile in a given spectral window is applied. It is known that if the phase of the incident field is symmetric around a given frequency, the interference paths around this value are mostly destructive and hence lead to a strong decrease of the nonlinear two-photon excitation [55]. In contrast, if the phase is of odd dependence around this frequency, then the two-photon excitation efficiency should be maximal, as in the case of a flat spectral phase. This scheme is applied to the previous picture of two spectral windows centered, respectively, on ω_1 and ω_2. The resulting SFG efficiency at the coupling polarization component $\omega_1 + \omega_2$ is therefore dependent on the spectral phase $\varphi_1(\omega) + \varphi_2(\omega)$, with $\varphi_1(\omega)$ and $\varphi_2(\omega)$ being the spectral-phase dependence of both components of the incident field. By setting the phase dependence such as it presents a symmetric point at both positions ω_1 and ω_2 but having opposite extrema [Fig. 7(a)], then the intrapulse interference will be constructive at the SFG position $\omega_1 + \omega_2$ where the phase sum is flat, while being destructive at $2\omega_1$ and $2\omega_2$ [Fig. 7(c)]. In contrast, by setting antisymmetric frequency dependencies with opposing slopes at ω_1 and ω_2 [Fig. 7(b)], constructive interference will occur at $2\omega_1$ and $2\omega_2$, while at $\omega_1 + \omega_2$ the signal will get canceled [Fig. 7(d)]. This effect has been observed experimentally on a KTP crystal (Fig. 7) with a good agreement with the expected response. The remaining SFG signal in the destructive interference regions seen in Fig. 7 is due to intrinsic limitations of this technique when dealing with large spectral excitation widths in molecular media [56]. This scheme nevertheless offers the possibility of manipulating the diagonal and nondiagonal coupling contributions mentioned above. In particular, it allows us to work with a complete spectral integration by a detector without the need of spectral filtering, leading to enhanced structural contrast imaging by accentuating specific tensorial components of the SFG response relative to other ones.

V. CONCLUSION

We have shown that polarization spectral shaping can provide an independent readout of particular SFG tensorial components from a single spectral measurement. This method permits the retrieval of unique information in molecular media related to molecular orientation and disorder that cannot be measured from traditional polarimetric measurements without additional data processing. The possible imaging of such individual components brings new possibilities for high-contrast structural spatial investigation with submicrometric resolution, which can be eventually dynamic. The additional phase shaping of the polarization-controlled pulse further shows that possible contrasts are reachable without spectral extraction of the signals. This technique can be applied to the study of any 2D symmetry in the sample plane. Extensions are also possible to other contrasts such as higher harmonics generation or on nonlinear fluorescence excitation where multiple spectral pathways are involved.

ACKNOWLEDGMENTS

The authors thank Dan Oron and Yaron Silberberg for fruitful and inspiring discussions, as well as Heykel Aouani for help with the preliminary measurements under far field conditions. This work is supported by the French National Research Agency under the program JC 2007, Project NLO-Shaping JC07-195504.

[1] C. K. Chen, T. F. Heinz, D. Ricard, and Y. R. Shen, Chem. Phys. Lett. **83**, 455 (1981).
[2] S. Roth and I. Freund, Biopolymers **20**, 1271 (1981).
[3] J. Gannaway and C. J. R. Sheppard, Opt. Quant. Elec. **10**, 435 (1978).
[4] I. Freund, M. Deutsch, and A. Sprecher, Biophys. J. **50**, 693 (1986).
[5] M. Flörsheimer, M. Bösch, C. Brillert, M. Wierschem, and H. Fuchs, Adv. Mater. **9**, 1061 (1997).
[6] C. Anceau, S. Brasselet, and J. Zyss, Chem. Phys. Lett. **411**, 98 (2005).
[7] M. Flörsheimer, R. Paschotta, U. Kubitscheck, C. Brillert, D. Hofmann, L. Heuer, G. Schreiber, C. Verbeek, W. Sohler, and H. Fuchs, Appl. Phys. B **67**, 593 (1998).
[8] Y. Shen, P. Markowicz, J. Winiarz, J. Swiatkiewicz, and P. N. Prasad, Opt. Lett. **26**, 725 (2001).
[9] S. Brasselet, V. Le Floc'h, F. Treussart, J.-F. Roch, J. Zyss, E. Botzung-Appert, and A. Ibanez, Phys. Rev. Lett. **92**, 207401 (2004).
[10] P. J. Campagnola, M. D. Wei, A. Lewis, and L. M. Loew, Biophys. J. **77**, 3341 (1999).
[11] L. Moreaux, O. Sandre, and J. Mertz, J. Opt. Soc. Am. B **17**, 1685 (2000).
[12] R. LaComb, O. Nadiarnykh, and P. J. Campagnola, Biophys. J. **94**, 4504 (2008).
[13] M. Strupler, M. Hernest, C. Fligny, J.-L. Martin, P.-L. Tharaux, and M.-C. Schanne-Klein, J. Biomed. Optics **13**, 054041 (2008).
[14] T. Yasui, Y. Takahashi, M. Ito, S. Fukushima, and T. Araki, Appl. Opt. **48**, D88 (2009).
[15] D. A. Dombeck, K. A. Kasischke, H. D. Vishwasrao, M. Ingelsson, B. T. Hyman, and W. W. Webb, Proc. Natl. Acad. Sci. USA **100**, 7081 (2003).
[16] E. Ralston, B. Swaim, M. Czapiga, W.-L. Hwu, Y.-H. Chien, M. G. Pittis, B. Bembi, O. Schwartz, P. Plotz, and N. Raben, J. Struct. Biol. **162**, 500 (2008).
[17] D. Oron, E. Tal, and Y. Silberberg, Opt. Lett. **28**, 2315 (2003).
[18] O. Masihzadeh, P. Schlup, and R. A. Bartels, Opt. Lett. **34**, 1240 (2009).
[19] K. Yoshiki, M. Hashimoto, and T. Araki, Jpn. J. Appl. Phys. **44**, L1066 (2005).
[20] K. Yoshiki, K. Ryosuke, M. Hashimoto, N. Hashimoto, and T. Araki, Opt. Lett. **32**, 1680 (2007).
[21] E. Y. S. Yew and C. J. R. Sheppard, Opt. Commun. **275**, 453 (2007).
[22] O. Masihzadeh, P. Schlup, and R. A. Bartels, Opt. Lett. **34**, 1090 (2009).
[23] S. Brasselet and J. Zyss, C. R. Phys. **8**, 165 (2007).
[24] V. Le Floc'h, S. Brasselet, J. Zyss, B. Cho, S. Lee, S. Jeon, M. Cho, K. Min, and M. Suh, Adv. Mater. **17**, 196 (2005).
[25] K. Komorowska, S. Brasselet, J. Zyss, L. Pourlsen, M. Jazdzyk, H. J. Egelhaaf, J. Gierschner, and M. Hanack, Chem. Phys. **318**, 12 (2005).
[26] V. L. Le Floc'h, S. Brasselet, J.-F. Roch, and J. Zyss, J. Phys. Chem. B **107**, 12403 (2003).
[27] P. Stoller, K. M. Reiser, P. M. Celliers, and A. M. Rubenchik, Biophys. J. **82**, 3330 (2002).
[28] T. Yasui, Y. Tohno, and T. Araki, Appl. Opt. **43**, 2861 (2004).
[29] T. Yasui, K. Sasaki, Y. Tohno, and T. Araki, Opt. Quantum Electron. **37**, 1397 (2005).
[30] R. M. Williams, W. R. Zipfel, and W. W. Webb, Biophys. J. **88**, 1377 (2005).
[31] C. Odin, Y. L. Grand, A. Renault, L. Gailhouste, and G. Baffet, J. Microsc. **229**, 32 (2008).
[32] E. J. Gualtieri, L. M. Haupert, and G. J. Simpson, Chem. Phys. Lett. **465**, 167 (2008).
[33] M. Kakehata, R. Ueda, H. Takada, K. Torizuka, and M. Obara, Appl. Phys. B **70**, S207 (2000).
[34] T. Brixner, G. Krampert, T. Pfeifer, R. Selle, G. Gerber, M. Wollenhaupt, O. Graefe, C. Horn, D. Liese, and T. Baumert, Phys. Rev. Lett. **92**, 208301 (2004).
[35] T. Suzuki, S. Minemoto, T. Kanai, and H. Sakai, Phys. Rev. Lett. **92**, 133005 (2004).
[36] F. Weise, S. M. Weber, M. Plewicki, and A. Lindinger, Chem. Phys. **332**, 313 (2007).
[37] C. G. Slater, D. E. Leaird, and A. M. Weiner, Appl. Opt. **45**, 4858 (2006).
[38] D. Oron, N. Dudovich, and Y. Silberberg, Phys. Rev. Lett. **90**, 213902 (2003).
[39] M. Aeschlimann, M. Bauer, D. Bayer, T. Brixner, F. J. G. de Abajo, W. Pfeiffer, M. Rohmer, C. Spindler, and F. Steeb, Nature (London) **446**, 301 (2007).

[40] T. Brixner and G. Gerber, Opt. Lett. **26**, 557 (2001).
[41] T. Brixner, G. Krampert, P. Niklaus, and G. Gerber, Appl. Phys. B **74**, s133 (2002).
[42] S. M. Weber, F. Weise, M. Plewicki, and A. Lindinger, Appl. Opt. **46**, 5987 (2007).
[43] M. Plewicki, F. Weise, S. M. Weber, and A. Lindinger, Appl. Opt. **45**, 8354 (2006).
[44] L. Polachek, D. Oron, and Y. Silberberg, Opt. Lett. **31**, 631 (2006).
[45] O. Masihzadeh, P. Schlup, and R. A. Bartels, Opt. Express **15**, 18025 (2007).
[46] M. Müller, J. Squier, and G. J. Brakenhoff, Opt. Lett. **20**, 1038 (1995).
[47] J. Kunde, B. Baumann, S. Arlt, F. Morier-Genoud, U. Siegner, and U. Keller, J. Opt. Soc. Am. B **18**, 872 (2001).
[48] T. Baumert, T. Brixner, V. Seyfried, M. Strehle, and G. Gerber, Appl. Phys. B **65**, 779 (1997).
[49] T. Bäck, D. B. Fogel, and Z. Michalewicz, *Evolutionary Computation* (The Institute of Physics Publishing, 2000).
[50] D. Zeidler, Ph.D. thesis, Ludwig-Maximilians-Universität München, 2001.
[51] H. Vanherzeele and J. D. Bierlein, Opt. Lett. **17**, 982 (1992).
[52] B. Richards and E. Wolf, Proc. R. Soc. London Ser. A **253**, 358 (1959).
[53] E. Y. S. Yew and C. R. J. Sheppard, Opt. Express **14**, 1167 (2006).
[54] N. Sandeau, L. L. Xuan, D. Chauvat, C. Zhou, J.-F. Roch, and S. Brasselet, Opt. Express **15**, 16051 (2007).
[55] D. Meshulach and Y. Silberberg, Nature (London) **396**, 239 (1998).
[56] V. V. Lozovoy, I. Pastirk, K. A. Walowicz, and M. Dantus, J. Chem. Phys. **118**, 3187 (2003).